Journal of Computational Physics 228 (2009) 4182–4199

Contents lists available at ScienceDirect

Journal of Computational Physics

journal homepage: www.elsevier.com/locate/jcp

# A general strategy for the optimization of Runge–Kutta schemes for wave propagation phenomena

Matteo Bernardini, Sergio Pirozzoli *

*Università degli Studi di Roma "La Sapienza", Dipartimento di Meccanica e Aeronautica, Via Eudossiana 18, 00184 Roma, Italy*

ARTICLE INFO

*Article history:*
Received 8 September 2008
Received in revised form 17 February 2009
Accepted 19 February 2009
Available online 6 March 2009

*Keywords:*
Computational aeroacoustics
Runge–Kutta schemes
Optimized algorithms
Numerical dispersion
Numerical dissipation

ABSTRACT

We analyze optimized explicit Runge–Kutta schemes (RK) for computational aeroacoustics, and wave propagation phenomena in general. Exploiting the analysis developed in [S. Pirozzoli, Performance analysis and optimization of finite-difference schemes for wave propagation problems, J. Comput. Phys. 222 (2007) 809–831], we rigorously evaluate the performance of several time integration schemes in terms of appropriate error and cost metrics, and provide a general strategy to design Runge–Kutta methods tailored for specific applications. We present families of optimized second- and third-order Runge–Kutta schemes with up to seven stages, and describe their implementation in the framework of Williamson's 2*N*-storage formulation [J.H. Williamson, Low-storage Runge–Kutta schemes, J. Comput. Phys. 35 (1980) 48–56]. Numerical simulations of the 1D linear advection equation and of the 2D linearized Euler equations are performed to demonstrate the validity of the theory and to quantify the improvement provided by optimized schemes.



## 1. Introduction

In the past decades intense efforts in computational aeroacoustics (CAA) have been devoted to develop schemes with minimal numerical dissipation and dispersion. Ideal CAA schemes should be able to propagate over long distances and for long times acoustic disturbances with a broad range of length and time scales. High order schemes for CAA are generally based on a method-of-lines approach, whereby spatial and time discretization are handled sequentially. Most of the efforts have been directed on trying to improve the discretization of the space derivative operators. For this purpose Lele [3] proposed central compact schemes, which guarantee resolution properties in wavenumber space similar to spectral ones. Central approximations of the spatial derivatives have null dissipation error, and this is the reason for their superiority in CAA with respect to upwind schemes. The basic idea of compact schemes is to improve the resolution properties of derivative approximations by minimizing the difference between the exact and the discrete dispersion relation. A wide variety of "optimized" schemes for spatial discretization are available in the literature [3–6], with varying degree of success, but mostly based on the attempt to give up maximum formal order of accuracy in the representation of the derivatives while improving the behavior in wavenumber space.

The issue of time integration of the semi-discretized set of ordinary differential equations (ODE) associated with a given spatial discretization has received comparatively less attention. Time integration in CAA applications is usually performed by means of classical, explicit third- or fourth-order Runge–Kutta algorithms [7], because of their simplicity of implementation and relatively large stability limits. Given a general non-autonomous system of ODEs stemming from the semi-discretization of a conservation law, symbolically written as

* Corresponding author. Tel.: +39 06 44585202; fax: +39 06 4881759.
*E-mail addresses:* matteo.bernardini@uniroma1.it (M. Bernardini), sergio.pirozzoli@uniroma1.it (S. Pirozzoli).

0021-9991/$ - see front matter © 2009 Elsevier Inc. All rights reserved.
doi:10.1016/j.jcp.2009.02.032

$$\frac{d\mathbf{U}}{dt} = \mathbf{F}(\mathbf{U}(t), t), \tag{1}$$

where $\mathbf{U}$ is the vector of point unknowns at time $t$, the general form of an explicit $s$-stage, two-level RK scheme to advance from time $t^n$ to $t^n + k$ is

$$\mathbf{U}^{n+1} = \mathbf{U}^n + k\sum_{i=1}^{s} b_i \mathbf{K}_i, \tag{2a}$$

$$\mathbf{K}_i = \mathbf{F}\left(\mathbf{U}^n + k\sum_{j=1}^{i-1} a_{ij}\mathbf{K}_j, t^n + kc_i\right), \quad i = 1, \ldots, s, \tag{2b}$$

with

$$c_i = \sum_{j=1}^{i-1} a_{ij}. \tag{3}$$

The coefficients $a_{ij}$ and $b_i$ can be determined in such a way as to achieve a given formal order of accuracy and/or to improve the computational efficiency. For example, to derive RK schemes with up to third-order of accuracy, the following conditions [7] must be satisfied

$$(O1): \quad \sum_{i=1}^{s} b_i = 1, \tag{4a}$$

$$(O2): \quad \sum_{i=1}^{s} b_i c_i = \frac{1}{2}, \tag{4b}$$

$$(O3): \quad \sum_{i=1}^{s} b_i a_{ij} c_j = \frac{1}{6}, \tag{4c}$$

$$(O4): \quad \sum_{i=1}^{s} b_i c_i^2 = \frac{1}{3}, \tag{4d}$$

where $(On)$ indicates formulas controlling $n$th-order of accuracy.

A few attempts have been made to improve the performance of RK schemes, with the broad idea of minimizing the incurred dispersion and dissipation error. Hu et al. [8] introduced a class of Low-Dissipation and Dispersion Runge–Kutta (LDDRK) schemes by minimizing (a suitable norm of) the difference between the amplification factor of the RK scheme and the "true" amplification factor. Those authors considered (linearly) second-order accurate schemes with four and five stages and fourth-order accurate ones with six stages, and 3$N$-storage implementation (i.e. requiring memory allocation proportional to three times the number of ODEs to be solved). For nonlinear problems the accuracy of the schemes proposed by Hu et al. drops to second-order.

Low-storage implementation is an important issue in CAA because of the extensive computational resources required by wave propagation problems in large domains. Kennedy et al. [9] have derived low-storage, explicit Runge–Kutta schemes, that use from two to five registers of memory, and having accuracy from third- to fifth-order. Those authors optimized schemes across a broad range of properties, such as linear and nonlinear stability, accuracy efficiency, error control reliability, dissipation and dispersion errors.

Stanescu and Habashi [10] devised 2$N$-storage implementations of many RK schemes, which maintain the formal order of accuracy also for nonlinear operators, by exploiting Williamson's [2] formulation, and enforcing constraints deriving from order of accuracy, storage and resolution requirements. In particular, they provided a low-storage implementation of LDDRK schemes developed by Hu et al. [8].

An alternative low-storage implementation was introduced by Calvo et al. [11], who proposed optimized third- and fourth-order, five-stage schemes. Their optimization strategy is based on first maximizing the stability range of the algorithm, and then trying to improve the range of well-resolved Courant numbers. The same authors [12] also proposed a variant of the method whereby the coefficients of the scheme were determined so as to maximize the sum of the stability and the accuracy range.

Bogey and Bailly [13] developed optimized second-order, five- and six-stage RK schemes based on minimizing the sum of the norms of the dissipation and dispersion errors in a given range of frequencies. Their strategy was also used by Berland et al. [14] to derive an optimized fourth-order accurate (in nonlinear sense) low-storage RK algorithm with a wide stability range.

Ramboer et al. [15] brought spatial discretization into the analysis, and attempted to minimize the total dissipation and dispersion errors deriving from coupling with time integration. The formulation of Ramboer et al. has the main advantage of being applicable also to upwind type schemes, as opposed to conventional strategies based on the assumption of central spatial discretizations.

In this paper we present a novel procedure to "optimize" (in a sense that will be clarified) the performance of Runge–Kutta time integration schemes for specific applications dominated by linear, wave-like propagation of disturbances with a broad spectrum of wavenumbers. The optimization procedure is based on the analysis developed in Ref. [1] to assess the performance of finite-difference schemes for CAA.

The paper is organized as follows: In Section 2 we present the key ingredients to set up the problem of performance optimization. In Section 3 we introduce families of optimized, multi-stage RK schemes tailored for specific problems (hereafter referred to as ORK), and illustrate their implementation in a low-storage framework. In Section 4 we test the validity of the proposed strategy for a number of applications, including the linear advection equation and the linearized Euler equations.

## 2. Performance analysis of numerical schemes

In the present section we recall some of the results reported in Ref. [1], to highlight the key findings that can be exploited to develop optimized Runge–Kutta schemes. The model problem is the linear propagation (at constant phase speed $a$) of sinusoidal disturbances with wavelength $\lambda$ (and wavenumber $w = 2\pi/\lambda$) in a one-dimensional unbounded domain

$$\frac{\partial u}{\partial t} + a\frac{\partial u}{\partial x} = 0, \qquad u(x,0) = \hat{u}_0 e^{iwx}, \tag{5}$$

uniformly discretized both in space (with grid spacing $h$) and time (with time step $k$). Ref. [1] assumed $s$-stage Runge–Kutta time integration and (either explicit or implicit) finite-difference discretization of the spatial derivatives of the type (denoted in the following as C$P$p)

$$v'_j + \sum_{L=1}^{P} \alpha_L (v'_{j+L} + v'_{j-L}) = \frac{1}{h}\sum_{\ell=1}^{p} a_\ell (v_{j+\ell} - v_{j-\ell}), \tag{6}$$

where $v_j$ is the approximate solution of Eq. (5) at node $j$.

Let $E$ be the relative $L_2$ error norm of the computed solution at time $T = nk$, and let $C$ be the computational cost, defined as

$$E = \frac{|v(\cdot,T) - u(\cdot,T)|_2}{|u_0(\cdot)|_2} = \frac{\left(\frac{1}{\lambda}\int_{x_0}^{x_0+\lambda} |v(x,T) - u(x,T)|^2 \,\mathrm{d}x\right)^{1/2}}{\left(\frac{1}{\lambda}\int_{x_0}^{x_0+\lambda} |u_0(x)|^2 \,\mathrm{d}x\right)^{1/2}}, \tag{7}$$

$$C = sN_{\mathrm{op}} TL \frac{1}{kh}, \tag{8}$$

where $C$ is assumed to be proportional to the total number of points in the computational domain $(L/h)$, the number of operations/node required by Eq. (6) (say $N_{\mathrm{op}}$), the number of Runge–Kutta stages $(s)$ and the number of time steps $(T/k)$. One can arrive, with a few approximations, to the following expressions for normalized cost and error metrics

$$e(\varphi,\sigma) \equiv \frac{E}{(awT)} = \frac{|g(\varphi,\sigma) - e^{-i\sigma\varphi}|}{\sigma\ \varphi}, \tag{9}$$

$$c(\varphi,\sigma) \equiv \frac{C}{(awT)\cdot(wL)} = sN_{\mathrm{op}}\frac{1}{\sigma\varphi^2}, \tag{10}$$

where $\varphi = wh$ is the reduced wavenumber, $\sigma = ak/h$ is the Courant number, $(awT)$ is a measure of the number of wavelengths traveled by the wave in a time interval $T$, $(wL)$ is a measure of the number of wavelengths contained in the computational domain, and

$$g(\varphi,\sigma) = \sum_{m=0}^{s} \gamma_m (-i\sigma\Phi(\varphi))^m, \tag{11}$$

is the amplification factor of the difference scheme [16]. The spatial discretization enters the analysis through the modified wavenumber $\Phi(\varphi)$ [3], defined as

$$\Phi(\varphi) = \frac{\sum_{\ell=1}^{p} a_\ell \sin(\ell\varphi)}{1/2 + \sum_{L=1}^{P} \alpha_L \cos(L\varphi)}, \tag{12}$$

and time integration through the coefficients $\gamma_m$, which are related to the coefficients $a_{ij}$ and $b_i$ of the underlying Runge–Kutta algorithm (Eq. (2)). Indeed, in the case of a system of linear ODEs, i.e. assuming $\mathbf{F}(\mathbf{U}) = \lambda\mathbf{U}$, one has [10]

$$\begin{cases} \gamma_0 = 1, \\ \gamma_1 = \sum_i b_i, \\ \gamma_2 = \sum_i b_i c_i, \\ \gamma_m = \sum_{i,j,k,\ldots,q,r} b_i \underbrace{a_{ij}a_{jk}\ldots a_{qr}}_{m-2\ \mathit{times}} c_r, \qquad m = 3,\ldots,s. \end{cases} \tag{13}$$

Linearly $r$th-order RK accurate schemes (i.e. $r$th-order accurate for linear ODEs) are obtained by setting

$$\gamma_m = \frac{1}{m!}, \qquad m = 0, \ldots, r, \tag{14}$$

for which (11) is a $r$th-order Taylor series expansion of the "exact" amplification factor [7].

When dealing with multidimensional nonlinear propagation problems of broadband signals, the primary effect is to have a whole range of spatial scales, say $|w| \leqslant \bar{w}$, and propagation velocities, say $|a| \leqslant \bar{a}$ (which imply $\bar{\varphi} = \bar{w}h$ and $\bar{\sigma} = \bar{a}k/h$), and a different weight of $\varphi$ in the cost metric (the number of points scaling as $h^d$, where $d$ is the number of space dimensions). The formulas for the normalized cost and error can then be arranged as

$$\bar{c}_d(\bar{\varphi}, \bar{\sigma}) = sN_{\mathrm{op}} \frac{1}{\bar{\sigma}\bar{\varphi}^{d+1}}, \tag{15}$$

$$\bar{e}(\bar{\varphi}, \bar{\sigma}) = \frac{1}{\bar{\sigma}\bar{\varphi}} \cdot \max_{(\varphi,\sigma)\in[0,\bar{\varphi}]\times[0,\bar{\sigma}]} |g(\varphi, \sigma) - e^{-i\sigma\varphi}|. \tag{16}$$

The changes with respect to the single-scale, one-dimensional case are: (i) replacement of the "local" normalized error function $e$ in Eq. (9) with the "global" error $\bar{e}$, representing the maximum of $e$ in the entire range of relevant wavenumbers and Courant numbers; and (ii) replacement of $\varphi^2$ in Eq. (10) with $\bar{\varphi}^{d+1}$ in the cost metric.

Optimizing the performance of a given scheme (i.e. for given values of $s, N_{op}$) for a given problem amounts to requiring that the computational cost be minimum for a given error level; this can be achieved by specifying a target level (say $\varepsilon$) for the relative error, and finding a pair of values $\bar{\varphi}^*(\varepsilon), \bar{\sigma}^*(\varepsilon)$ that minimize the cost metric. To clearly illustrate the optimization procedure in Fig. 1 we report the iso-lines of the normalized global error $\bar{e}$ and the two-dimensional cost $\bar{c}_2$ in the $(\bar{\varphi}, \bar{\sigma})$ plane for the C23 spatial discretization (corresponding to $\alpha_1 = 334/899,\ \alpha_2 = 43/1798,\ a_1 = 1065/1798,\ a_2 = 1038/899,\ a_3 = 79/1798$), coupled with the classical fourth-order Runge–Kutta time discretization (RK4, corresponding to $\gamma_0 = 1,\ \gamma_1 = 1,\ \gamma_2 = 1/2,\ \gamma_3 = 1/6,\ \gamma_4 = 1/24$).

The determination of the optimal working points of a fully discretized scheme proceeds by looking for the conditions of least cost for given allowable error (or the opposite). Geometrically, this amounts to finding the right-most iso-cost curve intersecting a given iso-error curve, which implies tangency of the two families of curves at the optimal points. Note that, by virtue of its definition (see Eq. (15)) the normalized cost function is concave, and the normalized error function (see Eq. (16)) is (almost always) convex with respect to the $\bar{\varphi}, \bar{\sigma}$ axes. In addition, since the iso-cost lines are steeper than the iso-error lines at large $\sigma$, it follows that, for any iso-error curve there is a unique point in which a curve of the iso-cost family is tangent to it. One (sample) optimal working point is indicated with a bullet in Fig. 1.

Ref. [1] also showed that the global error can be expressed with good approximation as

$$\bar{e}(\bar{\varphi}, \bar{\sigma}) \approx \max(\bar{e}_s(\bar{\varphi}), \bar{e}_t(\bar{\sigma}\bar{\varphi})), \tag{17}$$

where $\bar{e}_s$ is the spatial error (i.e. the error in the case of exact time integration),

$$\bar{e}_s(\bar{\varphi}; a_\ell, \alpha_L) = \frac{1}{\bar{\varphi}} \max_{0\leqslant\varphi\leqslant\bar{\varphi}} |\Phi(\varphi) - \varphi|, \tag{18}$$

and $\bar{e}_t$ is the temporal error (i.e. the error in the case of exact space integration),

$$\bar{e}_t(\bar{z}; \gamma_m) = \frac{1}{\bar{z}} \max_{0\leqslant z\leqslant\bar{z}} \left| \sum_{m=0}^{s} \gamma_m (-iz)^m - e^{-iz} \right|, \tag{19}$$

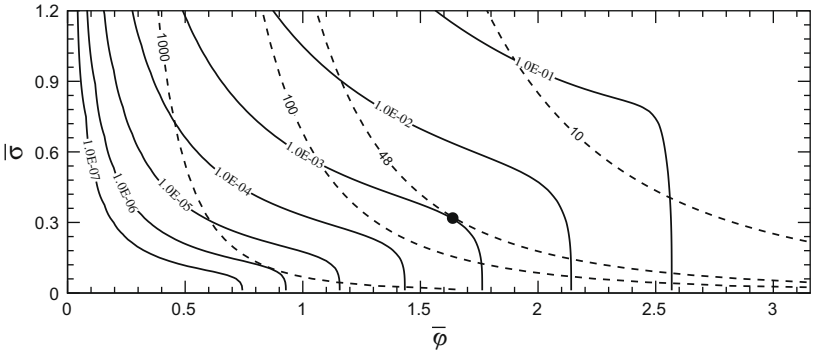


**Fig. 1.** Iso-contours of normalized "global" error $\bar{e}$ (Eq. (16), solid lines) and normalized two-dimensional cost $\bar{c}_2$ (Eq. (15), dashed lines) for C23 spatial discretization coupled with RK4 time integration. The upper boundary corresponds to $\bar{\sigma} = \sigma_{max}$ (as defined in Eq. (31)).

with $z = \sigma\varphi, \bar{z} = \bar{\sigma}\bar{\varphi}$. The condition of tangency of the iso-error and iso-cost curves for a normalized error level $\varepsilon$ under the approximation (17) is clearly realized when

$$\bar{e}_s(\bar{\varphi}) = \bar{e}_t(\bar{z}) = \varepsilon. \tag{20}$$

The validity of the approximate optimality condition (20) is checked in Fig. 2, where the error map reported in Fig. 1 is shown together with the corresponding approximation (17). The figure confirms that the "true" optimal points lie close to the points where Eq. (20) is satisfied.

The condition (20) can be used to determine the approximate optimal working conditions of a given scheme for a given problem, by separately considering the contributions of space- and time discretization, as follows:

(i) determine the optimal reduced wavenumber according to

$$\bar{\varphi}^*(\varepsilon) = \bar{e}_s^{-1}(\varepsilon); \tag{21}$$

(ii) determine the optimal Courant number from

$$\bar{\sigma}^*(\varepsilon) = \bar{z}^*(\varepsilon)/\bar{\varphi}^*(\varepsilon), \quad \bar{z}^*(\varepsilon) \equiv \bar{e}_t^{-1}(\varepsilon). \tag{22}$$

The normalized cost corresponding to the optimal working conditions is (see Eq. (15))

$$\bar{c}_d^*(\varepsilon) = sN_{\mathrm{op}} \frac{1}{\bar{z}^*(\varepsilon)\bar{\varphi}^{*d}(\varepsilon)}. \tag{23}$$

Eq. (23) suggests that the approximate analysis can also be exploited to develop new schemes. Indeed, optimized finite-difference schemes for a specified target error level $\varepsilon$ can be designed trying to maximize $\bar{\varphi}^*(\varepsilon)$ and $\bar{z}^*(\varepsilon)$ in Eq. (23), which amounts to separately optimize the spatial and time discretization schemes for the same error level.

## 3. Optimization of RK schemes

Our aim is improving the performance of explicit time integration schemes of Runge–Kutta type. For this purpose it is useful to split the overall algorithmic cost (as defined in Eq. (15)) as the product of the costs associated with the space- and the time- discretization, i.e.

$$\bar{c}_d(\bar{\varphi}, \bar{z}) = \bar{c}_t(\bar{z}) \cdot \bar{c}_{s_d}(\bar{\varphi}), \tag{24}$$

where $\bar{c}_t(\bar{z})$ and $\bar{c}_{s_d}(\bar{\varphi})$ are, respectively, the costs associated with time and space discretization

$$\bar{c}_t(\bar{z}) = \frac{s}{\bar{z}}, \qquad \bar{c}_{s_d}(\bar{\varphi}) = \frac{N_{\mathrm{op}}}{\bar{\varphi}^d}. \tag{25}$$

In particular, under the conditions of optimal performance (where Eq. (23) holds)

$$\bar{c}_t^*(\varepsilon) = \frac{s}{\bar{z}^*(\varepsilon)}, \qquad \bar{c}_{s_d}^*(\varepsilon) = \frac{N_{op}}{[\bar{\varphi}^*(\varepsilon)]^d}. \tag{26}$$

It is therefore apparent that time-optimized schemes (for a given target error $\varepsilon$) can be obtained by maximizing $\bar{z}^*(\varepsilon)$, which can be interpreted as a "temporal resolving efficiency" (in analogy with the spatial resolving efficiency, defined in Ref. [3]).

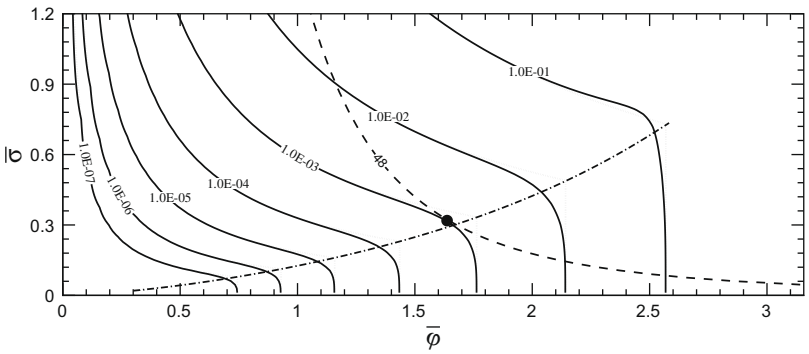


**Fig. 2.** Iso-contours of normalized "global" error $\bar{e}$ (Eq. (16), solid lines) and approximate error (Eq. (17), dots) for C23 spatial discretization coupled with RK4 time integration. Chained line represents the locus of approximate optimal working points (where Eq. (20) holds). The upper boundary corresponds to $\bar{\sigma} = \sigma_{max}$ (as defined in Eq. (31)).

Assuming for the moment exact spatial discretization, this requirement can be formally cast as

$$\bar{z}^*_{\rm opt}(\varepsilon) \equiv \max\{\bar{z} : \bar{e}_t(\bar{z};\gamma_m) \leqslant \varepsilon\}, \tag{27}$$

under the stability constraint of the RK algorithm

$$\zeta\bar{z}^*_{\rm opt}(\varepsilon) \leqslant \bar{z}_s, \tag{28}$$

where $\bar{z}_s$ is the stability limit

$$\bar{z}_s \equiv \max\{\bar{z} : |g_t(\bar{z};\gamma_m)| \leqslant 1\}, \tag{29}$$

being

$$g_t(\bar{z};\gamma_m) = \sum_{m=0}^{s} \gamma_m(-i\bar{z})^m, \tag{30}$$

the amplification factor in the case of null spatial error (corresponding to Eq. (11) for $\Phi \equiv \varphi$). The factor $\zeta$ is introduced in Eq. (28) to guarantee an extra stability margin beyond the range of well resolved $z$'s, which is important to exploit the advantages of improved time integration for practical purposes. In the present paper, $\zeta = 1.4$ is used, as it provides a good balance of performance and stability margin.

A numerical optimization procedure has been carried out to determine the coefficients $\gamma_m$ that maximize Eq. (27) under the constraint (28), based on standard ordered search in the parameter space in a sufficiently large neighborhood of the baseline values $1/m!$. RK schemes with different number of stages ($s = 4,\ldots,7$), and different target errors $\varepsilon = 10^{-n}(n = 3,\ldots,6)$ have been considered. Linear second-order formal accuracy has been imposed for four-, five- and six-stage schemes, while third-order accuracy has been imposed for seven-stage schemes. The optimized schemes thus obtained will be denoted in the following as ORKrs-n. The set of coefficients $\gamma_m$ determined from numerical optimization is reported in Table 1, together with the related stability margin and the optimal resolving efficiency, and in Fig. 3 we report the associated stability footprints (i.e. the locus of points in the complex $\bar{z}$ plane where $|g_t| = 1$). Note that, to emphasize deviations from standard RK, in Table 1 we actually report $1/m! - \gamma_m$.

The nominal performance of the ORK schemes is presented in Fig. 4 in terms of their temporal cost-error relations. The design working points of all schemes, i.e. the points where $\bar{z} = \bar{z}^*_{\rm opt}(\varepsilon)$ (and $\bar{c}_t = s/\bar{z}^*_{\rm opt}$), are indicated in the same figure with symbols. For comparison, in Fig. 4 we also report the curves associated with non-optimized (i.e. with maximum formal accuracy) RK schemes (hereafter denoted as RKs). Note that the maps corresponding to RK5 and RK6 are not reported, since the underlying schemes are unconditionally unstable. The figure confirms that schemes designed for a specific level of the relative error attain the least cost (among all schemes with the same number of stages) in the vicinity of the target error. The same reasoning can also be cast in terms of cost: ORK schemes deliver the least error near their design cost level (among all schemes of the family). The advantages offered by optimized schemes with respect to their non-optimized counterpart are particularly apparent when higher accuracy is required. For instance, for an error level $\varepsilon = 10^{-6}$, ORK24-6 and ORK37-6 offer a nominal reduction of the computational cost of about 35% respect to RK4 and RK7, whereas for a nominal error $\varepsilon = 10^{-3}$, ORK24-3 and ORK37-3 provide cost reduction of about 20%.

In order to compare ORK schemes with the RK schemes developed by previous authors, in the following we will consider: (i ) the second-order, five-stage scheme proposed by Hu et al. [8] (denoted as RK25-H); (ii) the third-order, five stage scheme

**Table 1**
Coefficients of time-optimized schemes for various target errors (for all schemes $\gamma_0 = 1,\ \gamma_1 = 1,\ \gamma_2 = 1/2$).

| Scheme | $1/3! - \gamma_3$ | $1/4! - \gamma_4$ | $1/5! - \gamma_5$ | $1/6! - \gamma_6$ | $1/7! - \gamma_7$ | $\bar{z}_s$ | $\bar{z}^*_{\rm opt}$ |
|---|---|---|---|---|---|---|---|
| ORK24-6 | $1.808\cdot10^{-4}$ | $1.808\cdot10^{-4}$ | – | – | – | 2.83 | 0.16 |
| ORK24-5 | $5.600\cdot10^{-4}$ | $5.600\cdot10^{-4}$ | – | – | – | 2.83 | 0.27 |
| ORK24-4 | $1.392\cdot10^{-3}$ | $1.392\cdot10^{-3}$ | – | – | – | 2.83 | 0.44 |
| ORK24-3 | $3.037\cdot10^{-3}$ | $3.037\cdot10^{-3}$ | – | – | – | 2.82 | 0.71 |
| ORK25-6 | $6.990\cdot10^{-5}$ | $9.065\cdot10^{-5}$ | $1.265\cdot10^{-3}$ | – | – | 3.47 | 0.26 |
| ORK25-5 | $2.000\cdot10^{-4}$ | $2.944\cdot10^{-4}$ | $1.152\cdot10^{-3}$ | – | – | 3.47 | 0.48 |
| ORK25-4 | $4.933\cdot10^{-4}$ | $8.759\cdot10^{-4}$ | $1.006\cdot10^{-3}$ | – | – | 3.49 | 0.85 |
| ORK25-3 | $1.098\cdot10^{-3}$ | $2.319\cdot10^{-3}$ | $9.983\cdot10^{-4}$ | – | – | 3.55 | 1.42 |
| ORK26-6 | $4.670\cdot10^{-5}$ | $4.924\cdot10^{-5}$ | $5.685\cdot10^{-4}$ | $5.648\cdot10^{-4}$ | – | 3.89 | 0.32 |
| ORK26-5 | $1.376\cdot10^{-4}$ | $1.426\cdot10^{-4}$ | $5.465\cdot10^{-4}$ | $4.608\cdot10^{-4}$ | – | 3.86 | 0.59 |
| ORK26-4 | $4.230\cdot10^{-4}$ | $4.229\cdot10^{-4}$ | $6.732\cdot10^{-4}$ | $4.441\cdot10^{-4}$ | – | 3.89 | 1.07 |
| ORK26-3 | $1.102\cdot10^{-3}$ | $1.102\cdot10^{-3}$ | $9.928\cdot10^{-4}$ | $4.280\cdot10^{-4}$ | – | 3.96 | 1.93 |
| ORK37-6 | 0 | $1.540\cdot10^{-5}$ | $-1.159\cdot10^{-6}$ | $3.920\cdot10^{-5}$ | $-4.480\cdot10^{-7}$ | 1.92 | 0.85 |
| ORK37-5 | 0 | $6.229\cdot10^{-5}$ | $-1.363\cdot10^{-5}$ | $8.472\cdot10^{-5}$ | $-1.012\cdot10^{-5}$ | 2.33 | 1.09 |
| ORK37-4 | 0 | $2.205\cdot10^{-4}$ | $-2.070\cdot10^{-5}$ | $1.510\cdot10^{-4}$ | $-4.390\cdot10^{-6}$ | 2.53 | 1.56 |
| ORK37-3 | 0 | $8.964\cdot10^{-4}$ | $8.939\cdot10^{-5}$ | $3.232\cdot10^{-4}$ | $3.197\cdot10^{-5}$ | 3.29 | 2.27 |

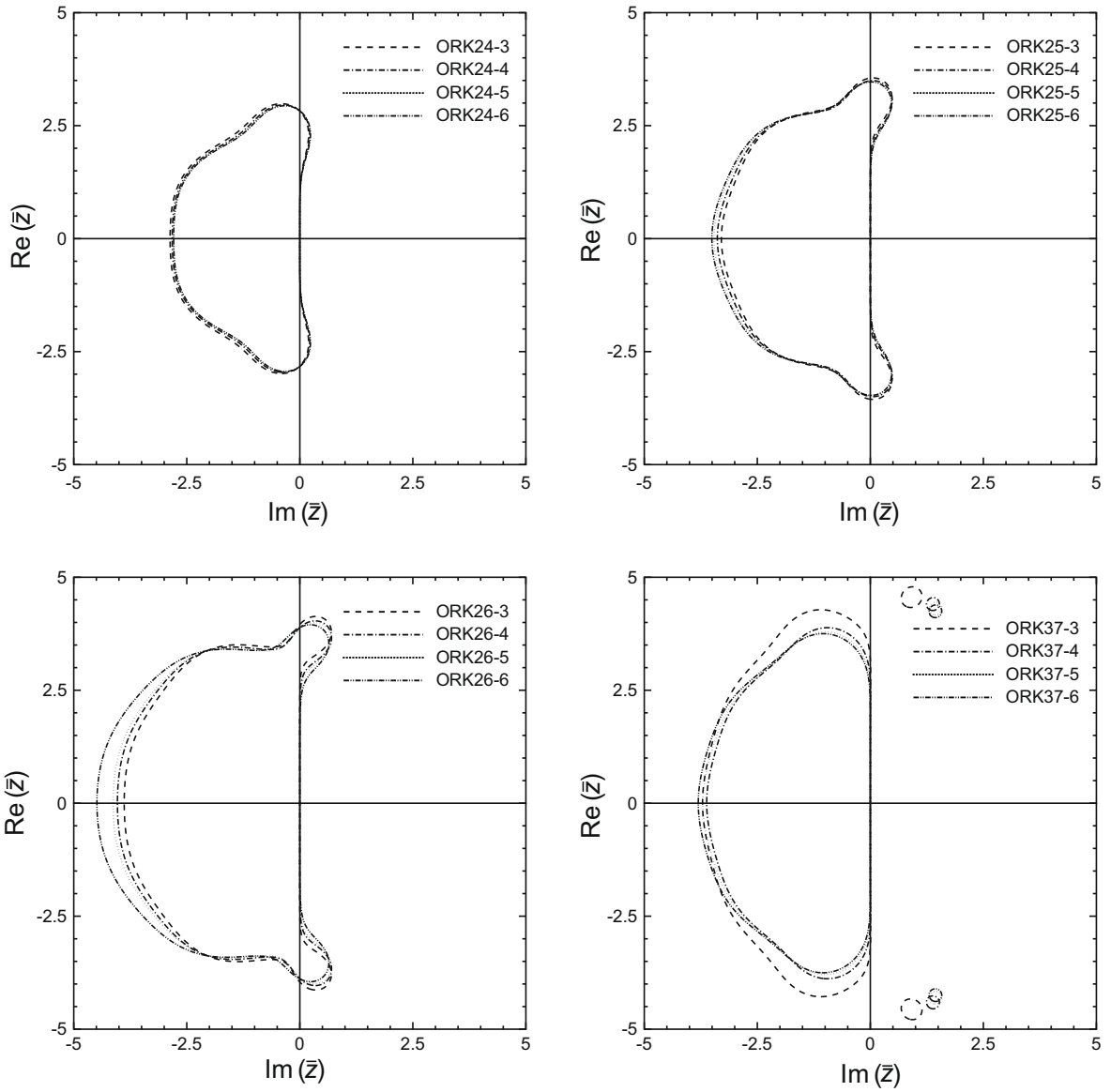


**Fig. 3.** Stability footprints of ORK schemes.

of Calvo et al. [11] (RK35-C); (iii) the second-order, five- and six-stage schemes proposed by Berland et al. [14] (RK25-B, RK26-B). The coefficients of those schemes are reported in Table 2, together with the related stability margin, and their nominal performance is analyzed in Fig. 5, in terms of the corresponding temporal cost-error relation. To clarify the advantages offered by the present ORK schemes, in the figure we also report the set of optimal working points associated with the present schemes (already shown in Fig. 4), and the envelope lines that represent, in a sense, the limit for the performance of ORK schemes with given number of stages and given formal order of accuracy. It is interesting to note that some of the schemes developed in the literature very nearly belong to the family of optimized schemes here discussed, even though they were devised following very different strategies. For instance, the RK25-H and RK25-B schemes have similar performance to ORK25-3, delivering optimal performance for $\bar{e}_t \approx 10^{-3}$, and the RK26-B scheme attains optimal performance for $\bar{e}_t \approx 2.3\mathrm{E}-4$. However, we observe that all schemes are largely inefficient if made to work away from their design conditions. While, for instance, the RK25-H and RK25-B schemes behave quite well for $\bar{c}_t \approx 3 \div 5$, they are not suitable for operating at larger cost values (or at smaller errors), where specifically designed schemes should be used. Looking through the existing literature, it appears that this fact has been largely disregarded, and RK schemes are very often used well away from their optimal performance point. From inspection of Fig. 5, we also observe that the efficiency steadily increases with the number of stages, and extremely efficient schemes are found for $s = 7$.

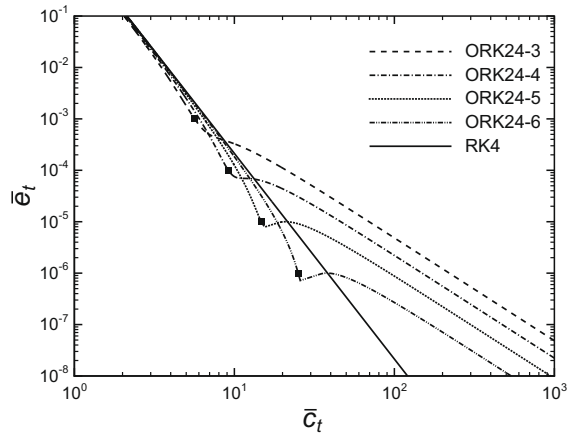


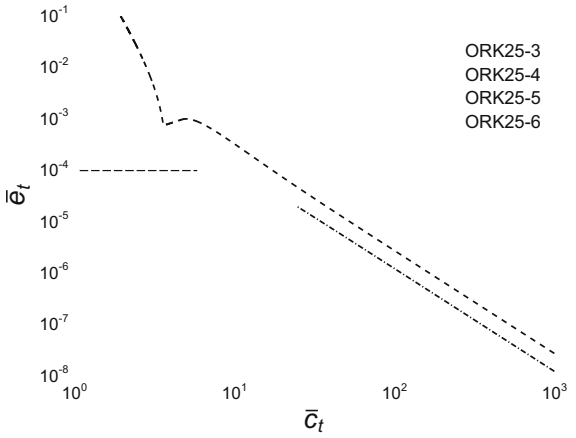


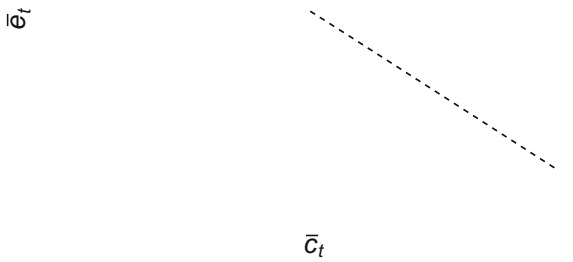


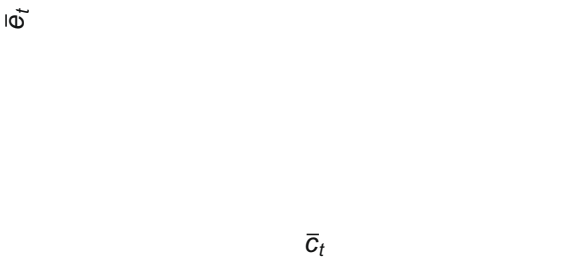


### 3.1. Coupling with finite accuracy spatial discretization

So far, time integration schemes have been evaluated assuming exact spatial discretization. However, the actual benefits of ORK schemes can only be assessed by including spatial discretization in the analysis. For the sake of the analysis we consider a central spatial discretization of the type (6) with $P = 2, p = 3$, which provides 10th-order accurate approximation of the spatial derivatives. The resolution properties of the C23 spatial discretization are shown in Fig. 6 in terms of modified wavenumber $\Phi(\varphi)$ and spatial cost-error $(\bar{c}_{s_d} - \bar{e}_s)$ relation.

We recall that optimal working points for a fully discretized scheme approximately correspond to the equality of the spatial and temporal errors, as stated in Eq. (20). Therefore, from the $\bar{c}_t - \bar{e}_t$ relation corresponding to a given RK scheme, and from the $\bar{c}_{s_d} - \bar{e}_s$ curve associated to a given spatial discretization (C23 in this case) the overall cost-error relation $\bar{c}_d^* - \varepsilon$ can be determined, from Eqs. (21)–(23). For instance, assuming $\varepsilon = 10^{-4}$ and ORK25-4 time integration, Fig. 4 yields $\bar{c}_t \approx 5.88$, and Fig. 6(b) yields $\bar{c}_{s_1} \approx 11.84$, giving an overall optimal cost $\bar{c}_1^* = \bar{c}_t \bar{c}_{s_1} \approx 69.62$. The optimal cost-error, cost-Courant

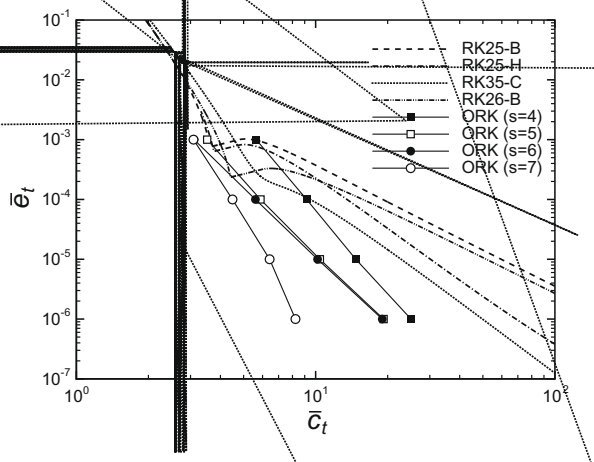


**Fig. 5.** Theoretical temporal cost-error relation for schemes developed by previous authors. Symbols denote optimal working points for the present family of ORK schemes.

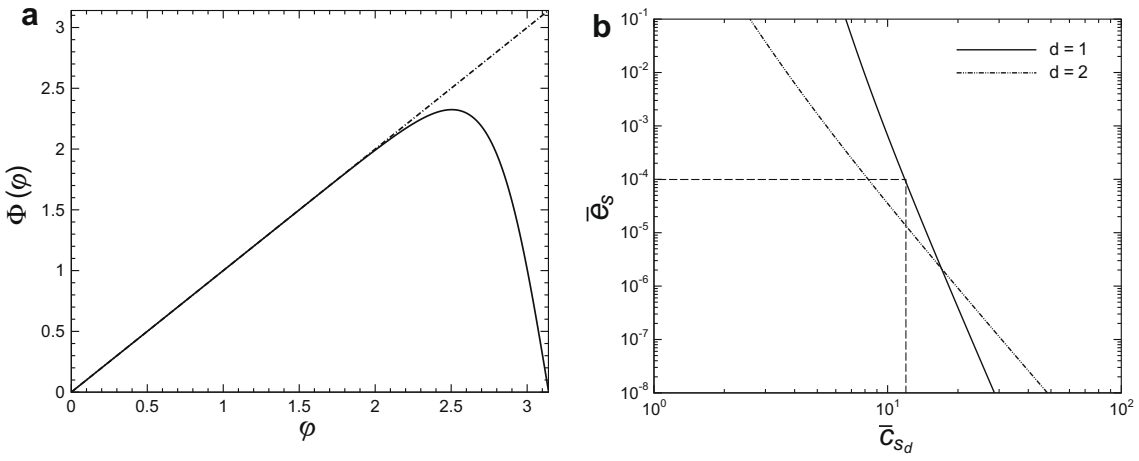


**Fig. 6.** C23 spatial discretization: modified wavenumber (a) and theoretical cost-error relation (b). Chained line in (a) indicates exact differentiation.

number and cost-reduced wavenumber maps are reported in Fig. 7 for standard and ORK schemes coupled with the C23 spatial discretization. The results obtained with different types of spatial discretization (not shown) follow the same qualitative behavior.

To correctly interpret the maps reported in Fig. 7 we observe that for any full discretization, a minimum value of cost exists for which it can be used under optimal conditions. Such value is dictated by the limit allowed by the CFL stability condition

$$\sigma_{max} = \frac{\bar{z}_s}{\max\limits_{\varphi\in(0,\pi)} \Phi(\varphi)}. \tag{31}$$

As a consequence, all maps in the figure are terminated at their leftmost cost level. The figure proves that (for any assigned spatial discretization) the use of multi-stage time discretization may provide improved efficiency. The figure also confirms that ORK schemes provide lower cost around their design error level, and allow working at lower values of cost compared to their non-optimized counterparts.

Fig. 7 provides useful guidance for the numerical computation of wave propagation problems. Indeed, given a fully discretized numerical scheme, for prescribed allowable error or affordable cost, the figure provides the set of $\bar{\varphi}^*, \bar{\sigma}^*$ to achieve optimal performance. From the optimal set $(\bar{\varphi}^*, \bar{\sigma}^*)$, one can directly derive the mesh spacing and the time step to perform the simulation. The figure also allows the choice of the "best" scheme for specific computational requirements. Similar maps to Fig. 7 can be determined for any fully discretized scheme in any number of space dimensions.

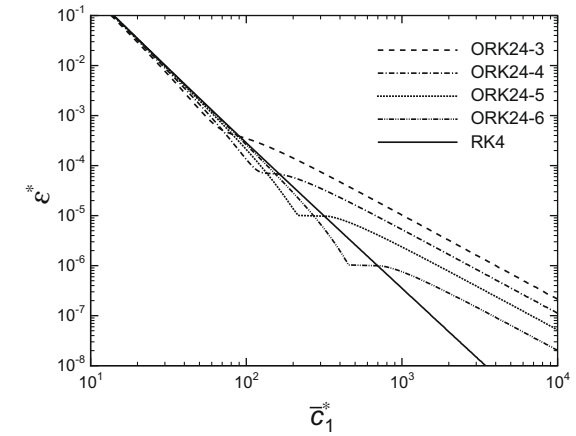


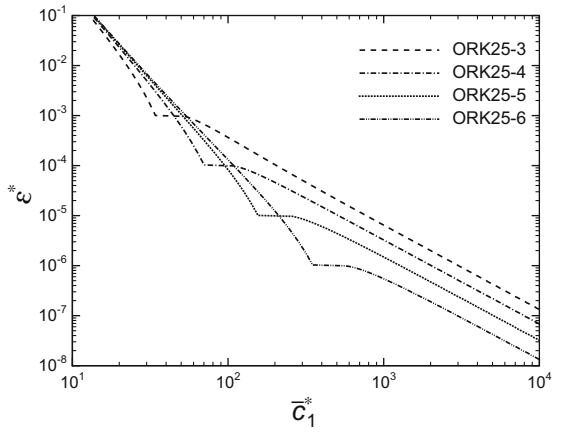


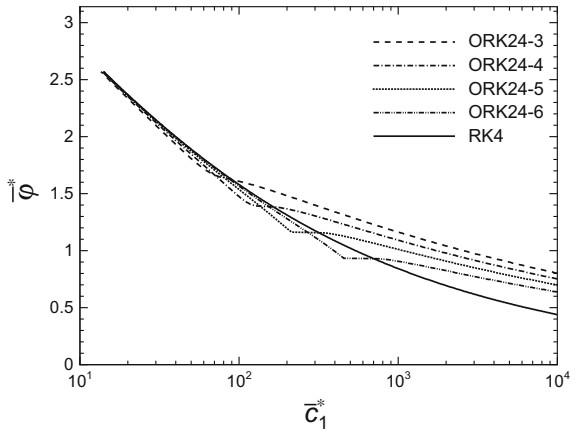


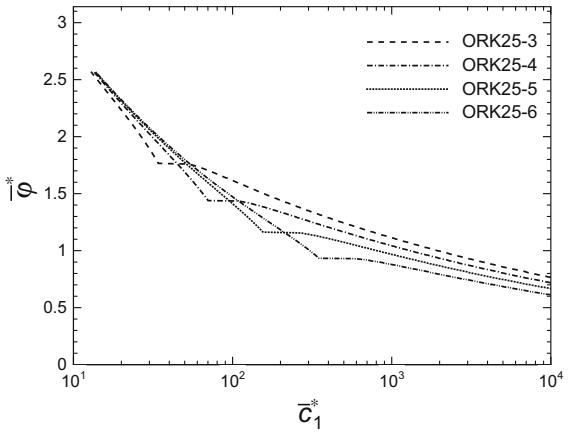


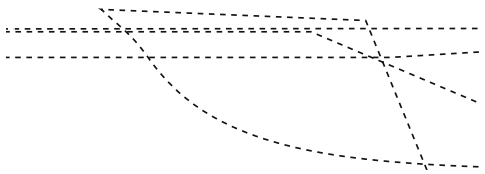

### 3.2. Low-storage implementation

Low-storage implementation of Runge–Kutta schemes is extremely important in computational aeroacoustics and direct numerical simulation of fluid turbulence, because of the extensive memory requirements. In this paper a 2*N*-storage RK implementation is considered [2,10]

$$\begin{aligned} \mathbf{W}_i &= \alpha_i \mathbf{W}_{i-1} + k\mathbf{F}(\mathbf{U}_{i-1}, t_i) \\ \mathbf{U}_i &= \mathbf{U}_{i-1} + \beta_i \mathbf{W}_i \end{aligned}, \qquad i = 1, \ldots, s, \tag{32}$$

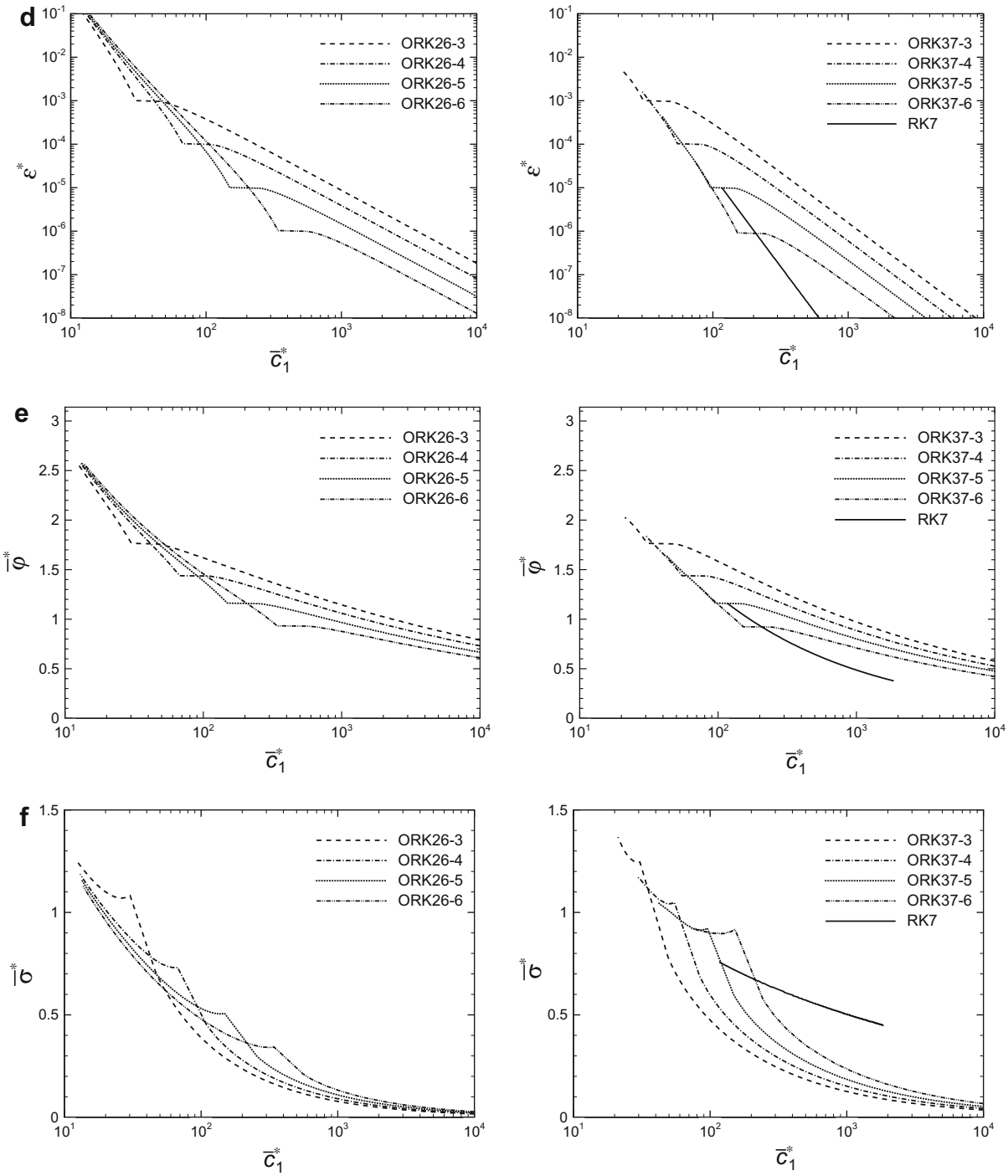


**Fig 7.** *(continued)*

where $\mathbf{U}_0 = \mathbf{U}^n,\ \mathbf{W}_0 = 0,\ \mathbf{U}_s = \mathbf{U}^{n+1},\ t_i = t^n + c_i k$, and the coefficients $\alpha_i, \beta_i$ are related to the coefficients $a_{ij}$ and $b_i$ in Eq. (2) through

$$\begin{cases} b_s = \beta_s, \\ b_{s-\ell} = \beta_{s-\ell} + \alpha_{s-\ell+1} b_{s-\ell+1}, \qquad \ell = 1, \ldots, s-1, \end{cases} \tag{33a}$$

$$\begin{cases} a_{i,i-1} = \beta_{i-1}, \\ a_{i,i-\ell} = \beta_{i-\ell} + \alpha_{i-\ell+1} a_{i,i-\ell+1}, \qquad \ell = 2, \ldots, i-1, \quad i = 2, \ldots, s. \end{cases} \tag{33b}$$

**Table 3**
Coefficients for low-storage implementation of ORK schemes.

| Scheme | $\beta_1$ | $\beta_2$ | $\beta_3$ | $\beta_4$ | $\beta_5$ | $\beta_6$ | $\beta_7$ |
|---|---|---|---|---|---|---|---|
| ORK24-6 | 0.336220070 | 0.7459839068 | 0.6637799293 | 0.2491852381 | – | – | – |
| ORK24-5 | 0.342225961 | 0.7378998064 | 0.6577740382 | 0.2474715291 | – | – | – |
| ORK24-4 | 0.355195767 | 0.7216228417 | 0.6448042325 | 0.2436826209 | – | – | – |
| ORK24-3 | 0.380005310 | 0.6945188216 | 0.6199946897 | 0.2360791597 | – | – | – |
| ORK25-6 | −0.228408869 | −0.3375294821 | 1.0584111324 | 0.5095230361 | 0.1699977380 | – | – |
| ORK25-5 | −0.297464891 | −0.2383372889 | 1.1238926915 | 0.5192262702 | 0.1735721998 | – | – |
| ORK25-4 | −0.415941679 | −0.1484922114 | 1.2363147896 | 0.5341909613 | 0.1796268900 | – | – |
| ORK25-3 | −0.442753070 | −0.1300855068 | 1.2563368334 | 0.5437722119 | 0.1864162368 | – | – |
| ORK26-6 | 2.408763770 | −0.0093047802 | −1.7331626235 | 0.6161831156 | 0.3243988527 | 0.1061189977 | – |
| ORK26-5 | 0.985053730 | −0.0876721057 | −0.3442717951 | 0.7290794182 | 0.3592180648 | 0.1191808143 | – |
| ORK26-4 | 0.887985566 | −0.1187527757 | −0.2573008677 | 0.7644450417 | 0.3693153010 | 0.1233269598 | – |
| ORK26-3 | 0.756825009 | −0.2013454676 | −0.1453692116 | 0.8528589966 | 0.3885442020 | 0.1308977071 | – |
| ORK37-6 | 0.404286428 | 0.3779647692 | 0.5206055649 | −0.2893735752 | -0.0806088372 | 0.7282311294 | 0.1557168440 |
| ORK37-5 | 0.401764550 | 0.3808976268 | 0.4821328765 | −0.4216138297 | -0.0484053163 | 0.8613273616 | 0.1645078891 |
| ORK37-4 | 0.383914682 | 0.3834155266 | 0.4859355191 | −0.4686050694 | -0.0395343652 | 0.9158170068 | 0.1696841636 |
| ORK37-3 | 0.301098150 | 0.4537177923 | 2.3848117585 | −0.0041723786 | -1.8255115482 | 0.4353716400 | 0.1396016403 |

Our objective is to cast the ORK schemes developed in the previous Section in terms of their $\gamma_m$ coefficients, in low-storage (32) form. For this purpose, using Eq. (33), one can rewrite Eq. (13) in terms of the coefficients $\alpha_i, \beta_i$, and obtain a nonlinear system of $s$ equations in $2s-1$ unknowns. To get a unique solution, in this paper we have set $\alpha_i = -1,\ i = 2,\ldots,s$, which yields a set of $s$ equations in $s$ unknowns. Explicit formulas for the coefficients $\beta_i$ as a function of $\gamma_m$ can be obtained up to $s = 6$ (with the symbolic manipulation software Mathematica). For example, for the case $s = 4$ one has

$$\beta_1 = \frac{\gamma_3 - 2\gamma_3^2 - 2\gamma_4}{\gamma_3 - 2\gamma_4}, \quad \beta_2 = \frac{-(\gamma_3 - 2\gamma_4)^2}{2\gamma_3(-\gamma_3 + 2\gamma_3^2 + 2\gamma_4)}, \quad \beta_3 = \frac{2\gamma_3^2}{\gamma_3 - 2\gamma_4}, \quad \beta_4 = \frac{\gamma_4}{\gamma_3}. \tag{34}$$

Since for the present ORK schemes $\gamma_1 = 1,\ \gamma_2 = 1/2$, second-order accuracy holds both in the linear and nonlinear case, since Eqs. (4a) and (4b) are satisfied. When $\gamma_3 = 1/6$ linearly third-order accurate schemes are obtained, and Eq. (4c) is satisfied. However, it is possible to verify (a posteriori) that for the present implementation Eq. (4d) is also automatically satisfied, thus providing third-order accuracy also in the nonlinear case. The full set of the low-storage coefficients $\beta_i$ are provided in Table 3 for all ORK schemes considered so far.

The set of coefficients $c_i$ (required in the case of non-autonomous ODE systems) is obtained from Eqs. (3) and (33b). In the special case $\alpha_i \equiv -1$ one has

$$c_1 = 0, \qquad c_i = c_{i-1} + [(-1)^i + 1]\frac{\beta_{i-1}}{2}, \quad i = 2,\ldots,s. \tag{35}$$

Note that such simple choice may lead to coefficients $c_i$ falling outside the natural range $[0,1]$. In that case, optimized schemes can still be cast in Williamson's low-storage form. Indeed, given the under-determination of the system (13), one can explicitly impose the constraints $c_i \in [0,1]$, giving up the requirement $\alpha_i \equiv -1$. For example, the ORK25-6 optimized scheme can be implemented in low-storage form using the set of coefficients listed in Table 4.

## 4. Numerical tests

### 4.1. Linear advection equation

To demonstrate the practical validity of the analysis developed in Section 3 we have performed a series of preliminary numerical simulations of the 1D linear advection equation with periodic boundary conditions.

First, we have considered the following initial condition (denoted as test A)

$$u_0(x) = \sin(10\pi x), \quad -1 \leqslant x \leqslant 1, \tag{36}$$

**Table 4**
Coefficients for low-storage implementation of ORK25-6 scheme enforcing $c_i \in [0,1]$.

| $i$ | $\alpha_i$ | $\beta_i$ | $c_i$ |
|---|---|---|---|
| 1 | 0.0 | 0.2 | 0.0 |
| 2 | −1.0 | 0.83204 | 0.2 |
| 3 | −1.55798 | 0.6 | 0.2 |
| 4 | −1.0 | 0.35394 | 0.8 |
| 5 | −0.45031 | 0.2 | 0.8 |

representing a sinusoidal monochromatic wave with wavelength $\lambda = 1/5$. Test case A exactly matches the conditions on which the theory is based, and it is aimed at numerically reproducing the findings of Section 3. A series of simulations have been performed at different values of the time step (and therefore of the temporal cost $\bar{c}_t$). The normalized relative $L_2$ error norm of the computed solution at time $T = 5$ has been evaluated according to (see Eqs. (7) and (9))

$$\tilde{e} = \frac{1}{\bar{w}aT}\left[\frac{\sum_j |v_j(T) - u(x_j, T)|^2}{\sum_j |u_0(x_j)|^2}\right]^{1/2}, \tag{37}$$

where $v_j$ and $u(x_j)$ are the numerical end the exact solution at node $x_j$, respectively. In order to single out the time discretization error, very high-order spatial discretization (up to 50th order) has been exploited at this stage, and genuine independence of the reported results upon the spatial discretization has been thoroughly checked. The computed temporal cost-error curves, obtained assuming (as obvious for this case) $\bar{w} = 10\pi$, are depicted in Fig. 8, where for illustrative purpose we only report the results for ORK schemes with $s = 4$ and $s = 5$. In the figure we also report the corresponding theoretical curves (already shown in Fig. 4). The figure proves self-consistency of the theoretical analysis. The differences near the dips of the error curves are due to the fact that a single wavenumber is present in the solution, and the incurred error is the "local" error, rather than the "global" one considered in the theory. The local error theoretical curves (not shown) exactly match the numerical data.

The second case under consideration is the propagation of a Gaussian pulse (denoted as B)

$$u_0(x) = \frac{1}{2}e^{-(x/3)^2}, \quad -50 \leqslant x \leqslant 50, \tag{38}$$

which has been frequently used [8,10–12] to evaluate the performance of numerical schemes for solutions with non-trivial content in Fourier space. To demonstrate the practical usefulness of ORK schemes in the case of finite spatial accuracy, simulations for test case B have been performed coupling time integration with the C23 spatial discretization, and working under conditions of nominal performance. Specifically, for a given cost level $\bar{c}_1$, the optimal Courant number $\bar{\sigma}^*$ and reduced wavenumber $\bar{\varphi}^*$ to perform the simulation have been selected from the diagrams reported in Fig. 7. A relevant length scale for test case B is the pulse diameter $\lambda = 6$, and accordingly we have set $\bar{w} = \pi/3$ to evaluate the normalized numerical error from Eq. (37). The computed cost-error relations thus obtained are reported in Fig. 9 for all ORK schemes. The shape of the maps is very similar to the theoretical curves of Fig. 7, and the optimal working points are located at the same positions in terms of cost; however, the error levels are all displaced to lower values. This is due to the fact that the actual numerical error is a weighted superposition of the error associated with the various harmonics that constitute the solution, while the theoretical error metric is based on a "worst case" assumption, i.e. the maximum error over the entire wavenumber range (see Eq. (16)). This observation confirms that, even though the theory is based on the analysis of monochromatic waves, it also yields significant insight into the behavior of more general types of solutions, and as such, it can be used as a guidance in the selection of RK schemes tailored for specific applications.

### 4.2. Linearized Euler equations

As a further step, we have considered the two-dimensional linearized Euler equations (LEE), which can be written in conservation form as

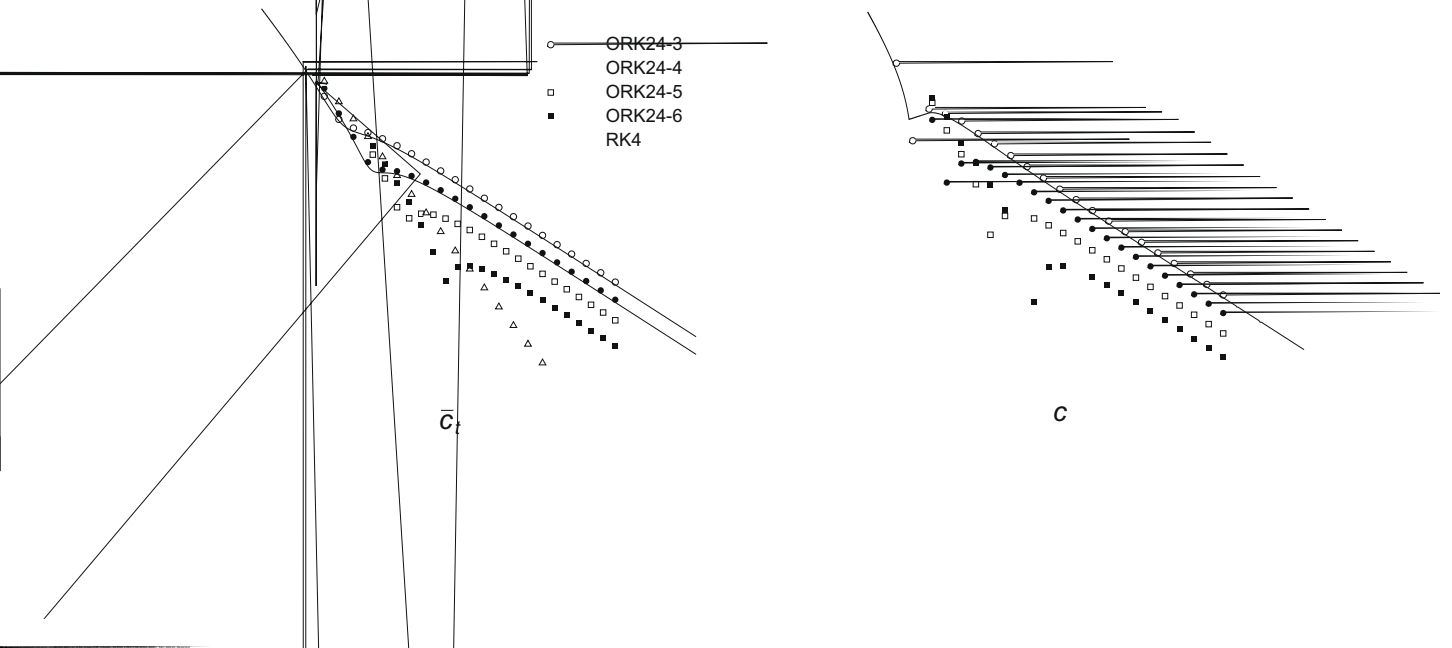

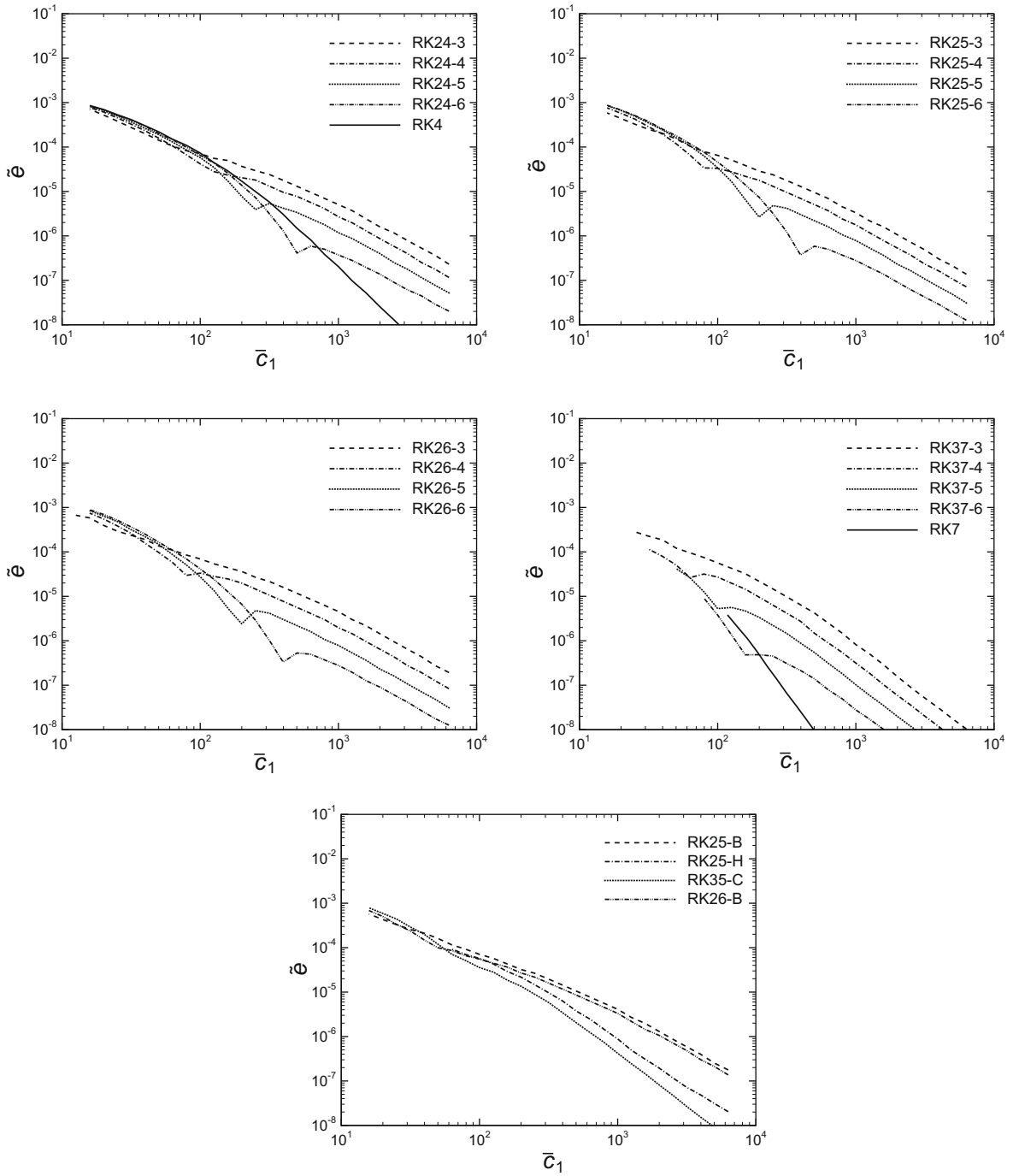


**Fig. 9.** Computed cost-error relation for test case B (C23 spatial discretization).

$$\frac{\partial \mathbf{q}}{\partial t} + \frac{\partial \mathbf{f}}{\partial x} + \frac{\partial \mathbf{g}}{\partial y} = 0, \tag{39}$$

where $\mathbf{q} = [u, v, p]^{\mathrm{T}}$, $\mathbf{f} = [p, 0, u]^{\mathrm{T}}$, $\mathbf{g} = [0, p, v]^{\mathrm{T}}$. The problem that we have considered (referred to as test case C in the following) is the reflection of a pressure pulse initially located at $(x_0 = 0, y_0 = 16)$ from a solid wall (located at $y = 0$). The initial conditions for the problem are

$$u = 0, \quad v = 0, \quad p = e^{-\alpha r^2}, \tag{40}$$

with $r = [(x-x_0)^2 + (y-y_0)^2]^{1/2}$ and $\alpha = \log 2/r_0^2,\ r_0 = 4$. The problem has the following exact solution at time $T$ [17]

$$\mathbf{q} = \begin{cases} u(x,y,T) = \frac{x}{2\alpha\eta} I_1 + \frac{x}{2\alpha\zeta} I_2, \\ v(x,y,T) = \frac{y-y_0}{2\alpha\eta} I_1 + \frac{y+y_0}{2\alpha\zeta} I_2, \\ p(x,y,T) = \frac{1}{2\alpha} I_3, \end{cases} \tag{41}$$

where $\eta = [x^2 + (y-y_0)^2]^{1/2},\ \zeta = [x^2 + (y+y_0)^2]^{1/2}$, and

$$\begin{aligned} I_1 &= \int_0^\infty e^{-\frac{\xi^2}{4\alpha}} \sin(\xi T) J_1(\xi\eta)\xi \,\mathrm{d}\xi, \\ I_2 &= \int_0^\infty e^{-\frac{\xi^2}{4\alpha}} \sin(\xi T) J_1(\xi\zeta)\xi \,\mathrm{d}\xi, \\ I_3 &= \int_0^\infty e^{-\frac{\xi^2}{4\alpha}} \cos(\xi T)[J_0(\xi\eta) + J_0(\xi\zeta)]\xi \,\mathrm{d}\xi, \end{aligned} \tag{42}$$

$J_0$ and $J_1$ being the zeroth- and first-order Bessel functions of the first kind, respectively. At the selected final time for the analysis ($T = 40$), the pulse has started to reflect from the bottom wall (as shown in Fig. 10). Gaussian quadratures have been exploited to evaluate the exact solution up to machine precision. Numerical simulations have been carried out in a rectangular computational domain $[-50, 50] \times [0, 100]$ discretized with square cells with size $h$. Nonreflecting boundary conditions are enforced at the left, right and top boundaries, and reflectional symmetry is exploited for the treatment of the bottom wall. The normalized $L_2$ error norm has been computed as

$$\tilde{e} = \frac{1}{\bar{w} a T} \left[ \frac{\sum_{i,j} |\mathbf{q}_{ij} - \mathbf{q}(x_i, y_j)|^2}{\sum_{i,j} |\mathbf{q}_0(x_i, y_j)|^2} \right]^{1/2}, \tag{43}$$

where $\mathbf{q}_{ij}$ is the numerical solution at the grid node $(x_i, y_j)$. The relevant wavenumber (associated with the initial pulse radius) is $\bar{w} = \pi/r_0$, and the characteristic propagation speed is $a = 1$.

Two different target cost values ($\bar{c}_2^* = 100$, and $\bar{c}_2^* = 25$) have been considered. As explained in the previous section, the best way to exploit the assigned computational resources is to preliminarily determine the optimal grid spacing and time step. The computed theoretical maps of optimal error, optimal Courant number and reduced wavenumber, reported in Fig 11, somewhat differ from the corresponding curves in Fig 7, because the cost metric is now evaluated in two space dimensions ($d = 2$). For example, considering the target cost $\bar{c}_2^* = 100$ for the ORK37-4 scheme, one has $\bar{\varphi}^* = 1.349,\ \bar{\sigma}^* = 0.485$, which implies $h^* = \bar{\varphi}^*/\bar{w} = 1.718, k^* = \bar{\sigma}^* h^*/a = 0.833$.

The computed error norms for the two selected target cost values are reported in Table 5a and b for a limited number of RK schemes coupled with C23 spatial discretization, together with the optimal $\bar{\varphi}, \bar{\sigma}$, and the nominal error. To highlight differences in the computed solutions, in Fig. 12 we also report the distribution of the local error on pressure at the bottom wall for a few representative schemes.

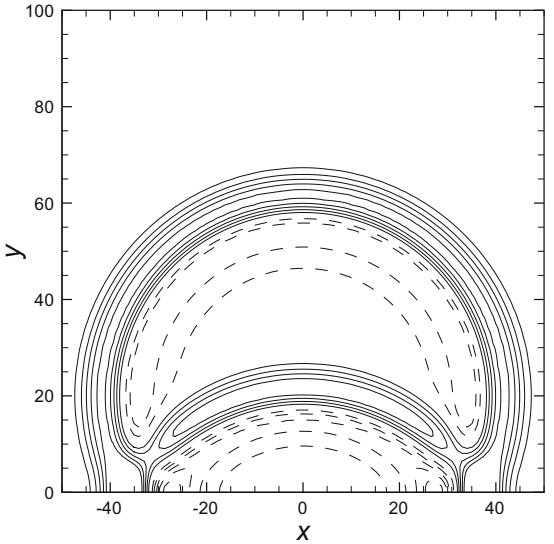


**Fig. 10.** Exact solution of test case C at time $T = 40$: 11 pressure contours from −0.1 to 0.1. Dashed lines indicate negative values.

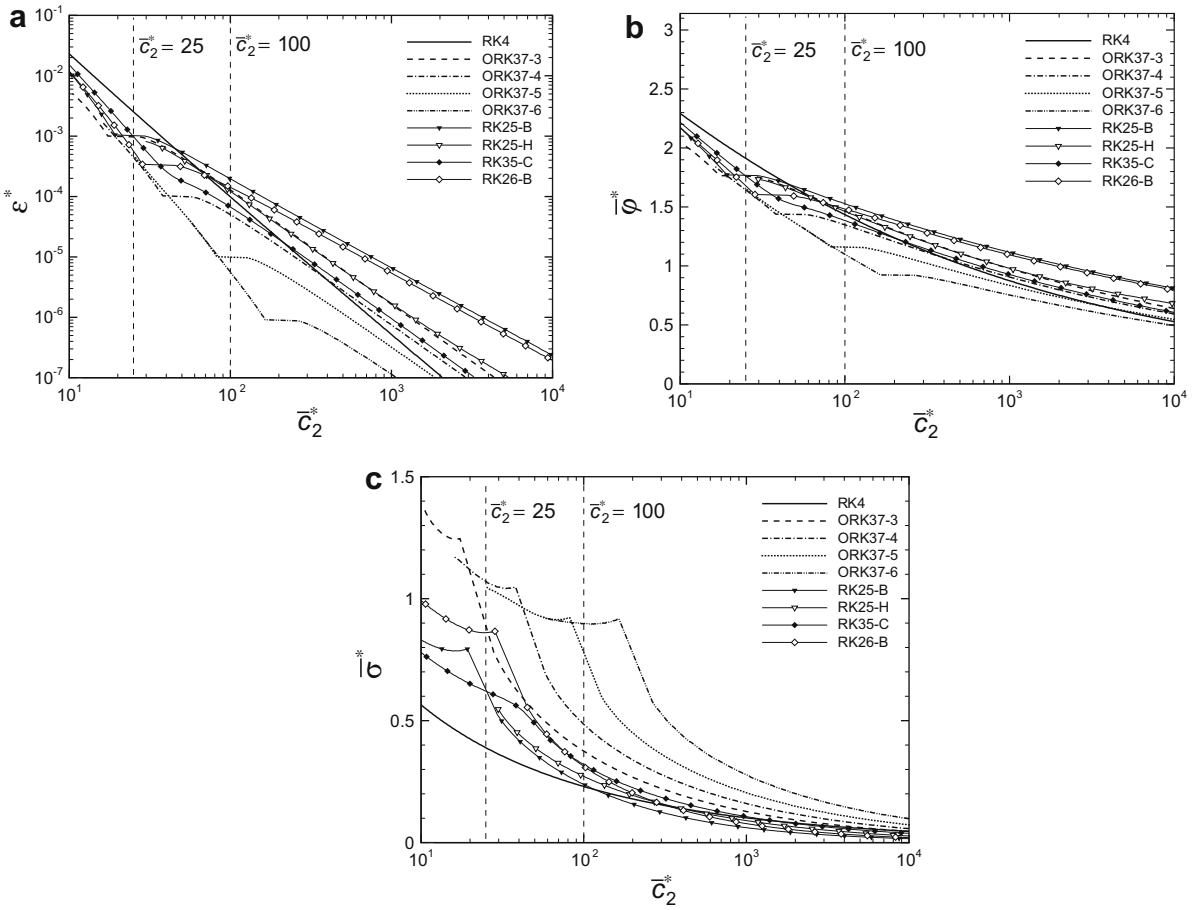


**Fig. 11.** Theoretical "optimal" error (a), Courant number (b), and reduced wavenumber (c) as a function of cost for ORK time integration schemes coupled with C23 discretization in two space dimensions.

**Table 5**
Test case C: optimal reduced wavenumber ($\bar{\varphi}^*$), Courant number ($\bar{\sigma}^*$), mesh spacing ($h^*$), time step ($k^*$), nominal error ($\varepsilon^*$) and computed error ($\bar{e}$) for given cost.

| ID | $\bar{\varphi}^*$ | $\bar{\sigma}^*$ | $h^*$ | $k^*$ | $\varepsilon^*$ | $\bar{e}$ |
|---|---|---|---|---|---|---|
| $\bar{c}_2^* = 100$ | | | | | | |
| RK4 | 1.435 | 0.230 | 1.827 | 0.420 | 9.856E−05 | 1.510E−05 |
| ORK37-3 | 1.469 | 0.375 | 1.870 | 0.701 | 1.283E−04 | 1.705E−05 |
| ORK37-4 | 1.349 | 0.485 | 1.718 | 0.833 | 5.013E−06 | 6.903E−06 |
| ORK37-5 | 1.156 | 0.770 | 1.472 | 1.133 | 9.933E−06 | 2.188E−06 |
| **ORK37-6** | **1.099** | **0.897** | **1.399** | **1.255** | **5.616E−06** | **7.452E−07** |
| RK25-B | 1.527 | 0.239 | 1.944 | 0.465 | 1.963E−04 | 2.872E−05 |
| RK25-H | 1.462 | 0.272 | 1.861 | 0.506 | 1.223E−04 | 1.682E−05 |
| RK35-C | 1.385 | 0.320 | 1.763 | 0.564 | 6.716E−05 | 9.792E−06 |
| RK26-B | 1.482 | 0.313 | 1.887 | 0.591 | 1.421E−04 | 2.202E−05c |
| ID | $\bar{\varphi}^*$ | $\bar{\sigma}*$ | $h^*$ | $k^*$ | $\varepsilon^*$ | $\bar{e}$ |
| $\bar{c}_2^* = 25$ | | | | | | |
| RK4 | 1.912 | 0.389 | 2.434 | 0.947 | 2.536E−03 | 3.118E−04 |
| ORK37-3 | 1.760 | 0.873 | 2.241 | 1.956 | 9.753E−04 | 1.803E−04 |
| **ORK37-4** | **1.644** | **1.071** | **2.093** | **2.242** | **4.500E−04** | **5.545E−05** |
| ORK37-5 | – | – | – | – | | |
| ORK37-6 | – | – | – | – | | |
| RK25-B | 1.740 | 0.625 | 2.215 | 1.384 | 1.023E−03 | 2.166E−04 |
| RK25-H | – | – | – | – | | |
| RK35-C | 1.763 | 0.621 | 2.245 | 1.394 | 9.850E−04 | 1.476E−04 |
| RK26-B | 1.680 | 0.861 | 2.139 | 1.842 | 5.706E−04 | 1.262E−04 |

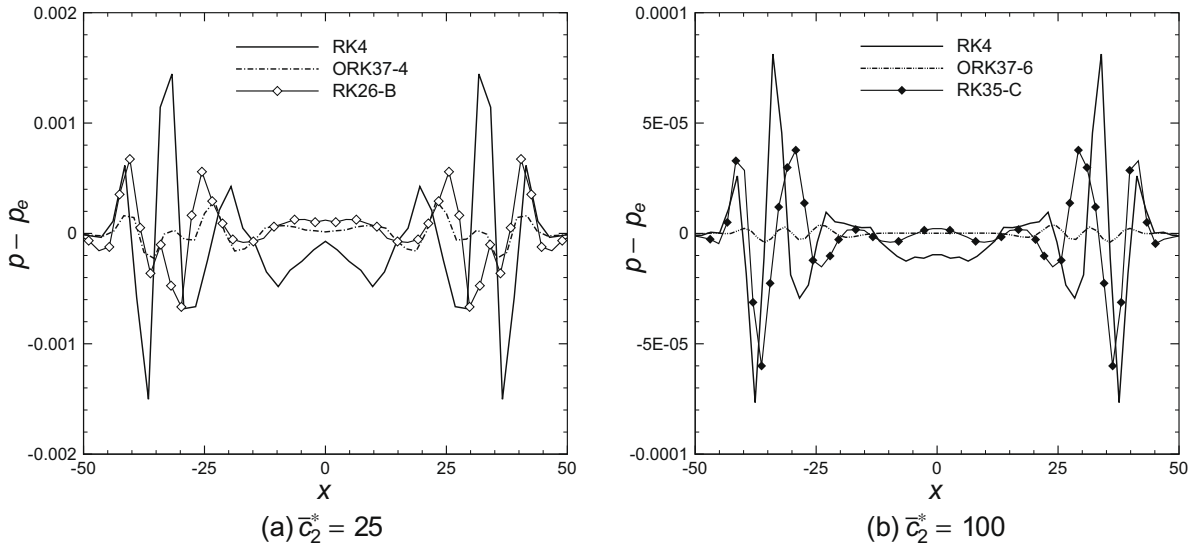


**Fig. 12.** Distribution of the local error on pressure along the bottom wall ($y = 0$) for a selection of RK schemes.

Considering the cost level $\bar{c}_2^* = 100$, from Table 5 and Fig. 12(a), the minimum nominal error is achieved using the ORK37-6 scheme. This expectation is confirmed by inspection of the normalized computed error. Specifically, the ORK37-6 scheme allows a reduction of at least a factor of twenty with respect to the optimized schemes proposed by other authors. This conclusion was to be expected on the basis of the discussion reported in Section 3, since those schemes are not suitable to operate at (relatively) high cost levels. We also observe that non-optimized, seventh-order RK scheme (RK7) cannot operate at the selected cost level, due to the limitation given by Eq. (31).

Carrying out the same analysis at lower cost level ($\bar{c}_2^* = 25$) leads to the results reported in Table 5b and Fig. 12(b). In this case the theory predicts best performance of the ORK37-4 scheme. This is again confirmed by the results of numerical simulations, even though in this case the gain with respect to existing optimized schemes is limited to a factor two. Again, this was to be expected, since the working point is close to the best performance of many existing RK schemes.

These considerations could be equally well carried out in terms of obtaining minimal cost for a given error level. In that case, one could enter Fig. 11 with a specified target error level to determine the optimal working conditions of a given scheme, and select the best candidate among available schemes to get the least possible cost.

## 5. Conclusions

We have presented a systematic procedure to determine the optimal performance of RK schemes (coupled with compact discretization of the spatial derivatives) for CAA applications, based on quantitative cost/error analysis. The analysis shows that, given a physical problem of wave propagation (characterized in terms of the maximum relevant wavenumber and maximum propagation speed), and given a spatial/temporal discretization, an optimum set of the mesh spacing and time step exists which minimizes the computational effort for given error (or vice-versa).

Optimization of RK schemes amounts to get the least temporal cost (i.e. largest possible time step) for given error. A family of schemes with different number of stages (up to seven) have been developed for different target error levels. The optimized RK schemes here derived have been cast in 2*N* low-storage form, to allow for efficient implementation of large-scale wave propagation problems. The analysis shows that some of the RK schemes developed in the literature very nearly belong to the family of optimized schemes here discussed, even though they were devised following different strategies.

The actual advantages offered by optimized RK schemes are demonstrated by performing numerical solutions of the 1D linear advection equation and of the 2D linearized Euler equations. An improvement of efficiency of a factor of $2 \div 20$ with respect to existing RK schemes can be obtained, depending upon the allowed error for numerical solution.

The main limitation of the present analysis is that it does not strictly apply to problems where the selection of the grid spacing is dictated by physical constraints (i.e. related to the Kolmogorov lengthscale for fluid turbulence), and to computational grids with severe stretching. The ideal field of application of the theory is in large-scale, LEE computations. LEE are largely used in aeroacoustics to predict the far-field sound assuming the near-field solution (typically computed by means of full Navier–Stokes solvers) as a source term [18]. Computational grids for LEE are typically very simple, and have uniform or smoothly varying spacing, thus making the theory presented in the paper applicable with very good accuracy.

Our main message is that there is no "best" time integration scheme in absolute sense. The choice of the most suitable algorithm critically depends upon the working conditions, and has to be carried out by clever selection among several possible ones. The present paper is intended to provide some guidance to perform such choice.

## References


[1] S. Pirozzoli, Performance analysis and optimization of finite-difference schemes for wave propagation problems, J. Comput. Phys. 222 (2007) 809–831.
[2] J.H. Williamson, Low-storage Runge–Kutta schemes, J. Comput. Phys. 35 (1980) 48–56.
[3] S.K. Lele, Compact finite difference schemes with spectral-like resolution, J. Comput. Phys. 103 (1992) 16–42.
[4] C.K.W. Tam, J.C. Webb, Dispersion-relation-preserving finite difference scheme for computational acoustics, J. Comput. Phys. 107 (1993) 262–281.
[5] J. Kim, D. Lee, Optimized compact finite difference schemes with maximum resolution, AIAA J. 34 (5) (1996) 887–893.
[6] C. Lui, S.K. Lele, Direct numerical simulation of spatially developing, compressible, turbulent mixing layers, AIAA Paper 2001-0291.
[7] J.C. Butcher, The Numerical Analysis of Ordinary Differential Equations, Wiley, Chichester, 1987.
[8] F.Q. Hu, M.Y. Hussaini, J.L. Manthey, Low-dissipation and low-dispersion Runge–Kutta schemes for computational acoustics, J. Comput. Phys. 124 (1996) 177–191.
[9] C.A. Kennedy, M.H. Carpenter, R.M. Lewis, Low-storage, explicit Runge–Kutta schemes for the compressible Navier–Stokes equations, Appl. Numer. Math. 35 (2000) 177–219.
[10] D. Stanescu, W.G. Habashi, 2*n*-storage low dissipation and dispersion Runge–Kutta schemes for computational acoustics, J. Comput. Phys. 143 (1998) 674–681.
[11] M. Calvo, J.M. Franco, L. Rández, Minimum storage Runge–Kutta schemes for computational acoustics, Comput. Math. Appl. 45 (2003) 535–545.
[12] M. Calvo, J.M. Franco, L. Rández, A new minimum storage Runge–Kutta scheme for computational acoustics, J. Comput. Phys. 201 (2004) 1–12.
[13] C. Bogey, C. Bailly, A family of low dispersive and low dissipative explicit schemes for flow and noise computations, J. Comput. Phys. 194 (2004) 194–214.
[14] J. Berland, C. Bogey, C. Bailly, Low-dissipation and low-dispersion fourth-order Runge–Kutta algorithm, Comput. Fluids 35 (2006) 1459–1463.
[15] J. Ramboer, T. Broeckhoven, S. Smirnov, C. Lacor, Optimization of time integration schemes coupled to spatial discretization for use in CAA applications, J. Comput. Phys. 213 (2006) 777–802.
[16] C. Hirsch, Numerical Computation of Internal and External Flows, Wiley, New York, 1988.
[17] J.C. Hardin, J.R. Ristorcelli, C.K.W. Tam (Eds.), ICASE/LaRC Workshop on Benchmark Problems in Computational Aeroacoustics, NASA CP 3300, 2005.
[18] C. Bogey, C. Bailly, D. Juvé, Computation of flow noise using source terms in linearized Euler's equations, AIAA J. 40 (2002) 235–243.